

Ultrafast ultrasound localization microscopy for deep super-resolution vascular imaging

Claudia Errico^{1,2,3}, Juliette Pierre^{1,2,3}, Sophie Pezet^{4,5}, Yann Desailly^{1,2,3}, Zsolt Lenkei^{4,5}, Olivier Couture^{1,2,3,*} & Mickael Tanter^{1,2,3,*}

Non-invasive imaging deep into organs at microscopic scales remains an open quest in biomedical imaging. Although optical microscopy is still limited to surface imaging owing to optical wave diffusion and fast decorrelation in tissue, revolutionary approaches such as fluorescence photo-activated localization microscopy led to a striking increase in resolution by more than an order of magnitude in the last decade¹. In contrast with optics, ultrasonic waves propagate deep into organs without losing their coherence and are much less affected by *in vivo* decorrelation processes. However, their resolution is impeded by the fundamental limits of diffraction, which impose a long-standing trade-off between resolution and penetration. This limits clinical and preclinical ultrasound imaging to a sub-millimetre scale. Here we demonstrate *in vivo* that ultrasound imaging at ultrafast frame rates (more than 500 frames per second) provides an analogue to optical localization microscopy by capturing the transient signal decorrelation of contrast agents—*inert* gas microbubbles. Ultrafast ultrasound localization microscopy allowed both non-invasive sub-wavelength structural imaging and haemodynamic quantification of rodent cerebral microvessels (less than ten micrometres in diameter) more than ten millimetres below the tissue surface, leading to transcranial whole-brain imaging within short acquisition times (tens of seconds). After intravenous injection, single echoes from individual microbubbles were detected through ultrafast imaging. Their localization, not limited by diffraction, was accumulated over 75,000 images, yielding 1,000,000 events per coronal plane and statistically independent pixels of ten micrometres in size. Precise temporal tracking of microbubble positions allowed us to extract accurately in-plane velocities of the blood flow with a large dynamic range (from one millimetre per second to several centimetres per second). These results pave the way for deep non-invasive microscopy in animals and humans using ultrasound. We anticipate that ultrafast ultrasound localization microscopy may become an invaluable tool for the fundamental understanding and diagnostics of various disease processes that modify the microvascular blood flow, such as cancer, stroke and arteriosclerosis.

The recent discovery of super-resolution optical microscopy led to a revolutionary improvement of resolution through the use of different technical approaches^{1,2}. One major implementation, fluorescence photo-activated localization microscopy (FPALM), exploits the stochastic blinking of specific fluorescent sources to separate them into individual events in independent frames. A super-resolved image is obtained by localizing the centre of each separable source and accumulating these positions over thousands of acquisitions. The resulting image highlights structures that are hundreds of times smaller than the wavelength, such as the cell membrane and small organelles³.

In clinical ultrasound imaging, intravenously injected contrast agents (1–3- μ m-diameter microbubbles) act as intravascular acoustic

sources to reveal the vascular bed. At typical concentrations, a cloud of microbubbles can be considered as a sub-wavelength random distribution of Rayleigh scatters. The resolution of ultrasound contrast imaging is limited by the classical wave diffraction theory and corresponds roughly to the ultrasonic wavelength (typically between 200 μ m and 1 mm in clinical applications). Nevertheless, thanks to the advent of ultrafast ultrasound imaging⁴, we recently proposed an ultrasound equivalent of FPALM^{5,6} that surpassed the conventional diffraction limit of echography by more than tenfold. The use of ultrafast acquisitions based on plane wave transmissions at the rate of a thousand frames per second may lead to several key advantages when imaging contrast agents. First, the decorrelation of the microbubble signal from frame to frame is typically in the millisecond range⁷. As the tissue signature decorrelates more slowly than the microbubble signal, it is thus removed by simply applying a differential subtraction filter of consecutive frames. Second, since they respond to ultrasound differently over several frames, microbubbles blink separately through the spatiotemporal differentiation process and become temporally separable sources. Last, since the ultrasonic sequence provides simultaneously very high temporal resolution in all pixels of the image, it becomes possible to track the signature of many individual microbubbles both in space and time and thus to quantify the local blood flow speed over a very large dynamical range. As ultrasonic waves can penetrate several centimetres of tissue, extracting the positions of each of these bubbles could lead to the full reconstruction of the deep vascular system down to the level of capillaries. However, the usefulness of these theoretical benefits remains to be demonstrated *in vivo*.

Current methods for *in vivo* microvascular imaging are limited by trade-offs between the depth of penetration, resolution and acquisition time. For instance, microcomputed tomography⁸ and magnetic resonance imaging⁹ are able to resolve vessels down to a few tens of micrometres with deep tissue penetration, but they remain limited by long scanning times. Near-infrared II fluorescence imaging¹⁰ has high spatial resolution (~50 μ m) and fast acquisition times (<200 ms). Nevertheless, it lacks sufficient tissue penetration (<1–3 mm) for whole-brain imaging. High-resolution photoacoustic imaging¹¹ does not require contrast agents and can attain resolutions of a few micrometres, but also lacks penetration (0.75 mm). Finally, acoustic angiography resolves tumour vessels around 150 μ m in diameter, but is still hampered by the trade-off between penetration and resolution¹².

Here, we demonstrate ultrafast ultrasound localization microscopy (uULM), which combines deep penetration and super-resolution imaging at unprecedented spatiotemporal resolution, by using clinically approved contrast agents: *inert* gas microbubbles. uULM is implemented *in vivo* on anaesthetized male Sprague–Dawley rats fixed within a stereotactic frame. Their skull was either left intact or thinned to reduce the acoustic attenuation caused by the bone. We used a small

¹INSERM, Institut Langevin, 1 rue Jussieu, 75005 Paris, France. ²Institut Langevin, ESPCI-ParisTech, PSL Research University, 1 rue Jussieu, 75005 Paris, France. ³CNRS UMR 7587, 1 rue Jussieu, 75005 Paris, France. ⁴CNRS, UMR 8249, 10 rue Vauquelin, 75005 Paris, France. ⁵Brain Plasticity Unit, ESPCI-ParisTech, PSL Research University, 10 rue Vauquelin, 75005 Paris, France.

*These authors contributed equally to this work.

ultrasonic probe, connected to a fully programmable ultrafast ultrasound scanner to image a coronal slice of the brain.

The major challenge of ULM is to intercept a sufficient number of separable sources (microbubbles) in the blood stream to obtain super-resolved vasculature maps over a large region within a reasonable acquisition time. Therefore, we detected microbubbles in the rat brain cortex by looking at their fast decorrelation within a stack of 75,000 images acquired continuously for 150 s. The millisecond-timescale decorrelation of the microbubble signal can be generated by several processes, including disruption, dissolution and motion. In the current implementation, pulse sequences were chosen to reduce ultrasound-induced disruption or dissolution of microbubbles. As microbubbles are point-scatters and since small variations of phase can be detected in the radio-frequency data, microbubble displacement much smaller than the wavelength appears as a strong decorrelation signal on differential filtered images. Moreover, by exploiting the coherence of backscattered signals, the spatiotemporal filtering approach discriminates slowly moving objects of sub-wavelength size (low spatial coherence), that is, bubbles, from slow motion tissue signals whose temporal variations affect many neighbouring pixels the same way (high spatial coherence). The ultrafast frame rate was achieved by emitting plane waves and collecting the backscattered echoes with all the array elements. For each transmission, the resulting echoes were exploited to reconstruct *in silico* an entire ultrasonic frame by using parallel beamforming. In the averaged stack of ultrasound images only the thinned skull was observable (Fig. 1a). The decorrelation of bubbles was detected using frame-to-frame differential processing, which yields individual and fast-changing sources within the ultrafast ultrasound images (Fig. 1b). This high-pass filter uses the very high spatiotemporal sampling to eliminate tissue and skull signals. Since microbubbles are much smaller than the wavelength (1–3 μm versus 100 μm) and can be individually separated in space and time, they appeared as the point-spread function (PSF) of the ultrasound system. The spatial coordinates of the bubble centroids were extracted one by one by deconvolving the individual sources from the predicted Gaussian PSF. As these sources are locally unique, each of these positions can be estimated with a 2.5 μm maximum theoretical resolution in the axial direction. For example, a blinking microbubble flowing in vessels at the level of the primary somatosensory forelimb or hindlimb cortex (S1HL/FL), appeared as a spot representing the centre of the interpolated PSF (Fig. 1c).

Typically, we localized in 150 s about 1,000,000 events within one hemisphere of the brain cortex. Furthermore, we were able to track each moving bubble according to its instantaneous position and in-plane velocity vector, leading to quantitative and localized maps of cerebral blood flow velocity. Hence, ultrafast imaging allows the reconstruction of entire organs within tens of seconds, a prerequisite for a preclinical and clinical modality. Far beyond a technological leap, ultrafast imaging ensures the necessary discrimination between single bubble signatures and tissue at high bubble concentrations using optimal spatiotemporal clutter filters¹³. By tracking the local motion of bubbles at a kHz rate, it estimates their motion over a very large dynamic range of velocities and consequently vessel diameters (1 mm s^{-1} to several cm s^{-1} and 15 μm to 1–5 mm, respectively) during a sufficiently long acquisition time simultaneously in all voxels of the image. Finally, in fast-moving or pulsatile organs, tissue motion correction could be assessed through speckle tracking with micrometric sensitivity to co-register bubble positions in real time or post-processing^{5,14,15}. This remains a fundamental asset with respect to individual bubble localization techniques based on conventional ultrasound sequences, recently¹⁶ discussed, which need to separate echoes through high dilution of contrast agents and image clamped tissue for extended durations (1 h) because of limited frame rates¹⁷.

We obtained extremely detailed structural reconstructions of the microvasculature in the rat brain cortex (5 mm width and 3 mm

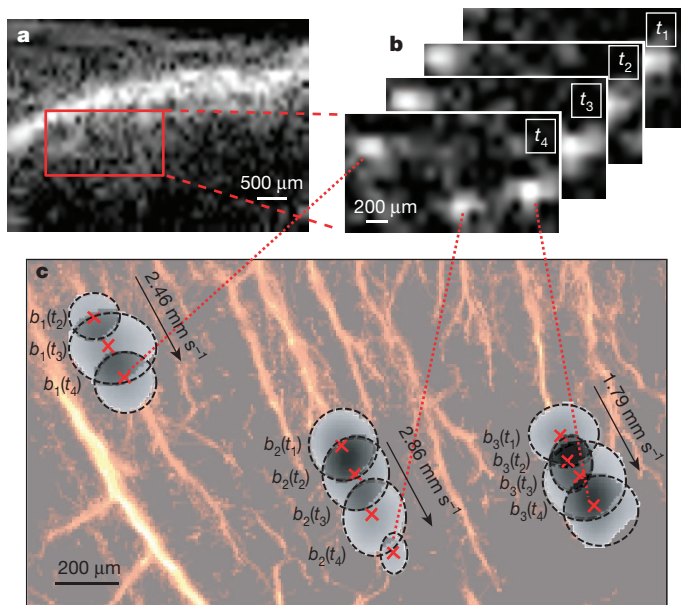


Figure 1 | Principle of uULM. **a**, Ultrafast detection of individual sources from a low-quality B-mode image (averaged stack of 250 beamformed images), through a thinned skull. **b**, Four representative frames were separated by 44 ms (t_1 – t_4) and filtered to remove the slow-moving tissue signal. **c**, Three independent microbubbles blinking over several milliseconds from **b** were followed in the region of interest within the cortex. The echo of each bubble event (high-contrast pixels) was deconvolved with the PSF to obtain the exact position of the centroid (red crosses). Superposition of thousands of occurrences yields a highly resolved localization map for this region.

depth) under the thinned skull window (Fig. 2a), displaying vessels with diameters between 15 μm and 65 μm . The images were reconstructed with a pixel size of 10 $\mu\text{m} \times 8 \mu\text{m}$, corresponding to a tenfold increase in resolution as compared to conventional ultrasound imaging. Furthermore, bifurcations of the penetrating arterioles within the S1HL/FL were easily observable down to the terminal branching points (Fig. 2a), where vessels attain the hypovascular white matter¹⁸. In comparison, the contrast-enhanced image created using conventional power Doppler is limited by diffraction (Fig. 2b)¹⁹, highlighting only the large vessels of the rat brain cortex without distinguishing details below the wavelength scale. Moreover, Doppler detection is strongly biased towards flows that are perpendicular to the array.

More detailed analysis of the cross-section of individual vessel profiles, indicated by lines 1 and 2 in Fig. 2a, yielded diameter sizes of 17 μm and 9 μm full-width at half-maximum, respectively, corresponding to capillaries²⁰ (Fig. 2c). These values represent a convolution between the actual size of the vessel and the response of the localization microscopy method, giving an upper limit to its resolution (wavelength $\lambda/10$). Investigation of a branching vessel profile (profile 3 in Fig. 2a) showed that at a distance of 16 μm ($\lambda/6$), the two vessels are still clearly separated. Such high resolution depends on the number of bubbles present in the reconstructed pixel (10 $\mu\text{m} \times 8 \mu\text{m}$) and could thus be further improved with longer integration times.

Next, we evaluated the ability of our method to measure blood flow dynamics in cortical microvessels. Measured blood flow in-plane velocities in the rat brain showed a large dynamic range up to several cm s^{-1} for large vessels and down to 2 mm s^{-1} in small vessels. Blood flow velocity inside of the relatively large penetrating artery was well resolved (profile 4 in Fig. 2d, e, profile 5 in Fig. 2d, f) and was inversely correlated with vessel diameter, showing 15 mm s^{-1} maximum velocity at 80 μm diameter and 2 mm s^{-1} maximum velocity at 15 μm diameter, consistent with the literature values^{21,22}. Interestingly, it was clear that larger vessels support higher flow within their centre with respect

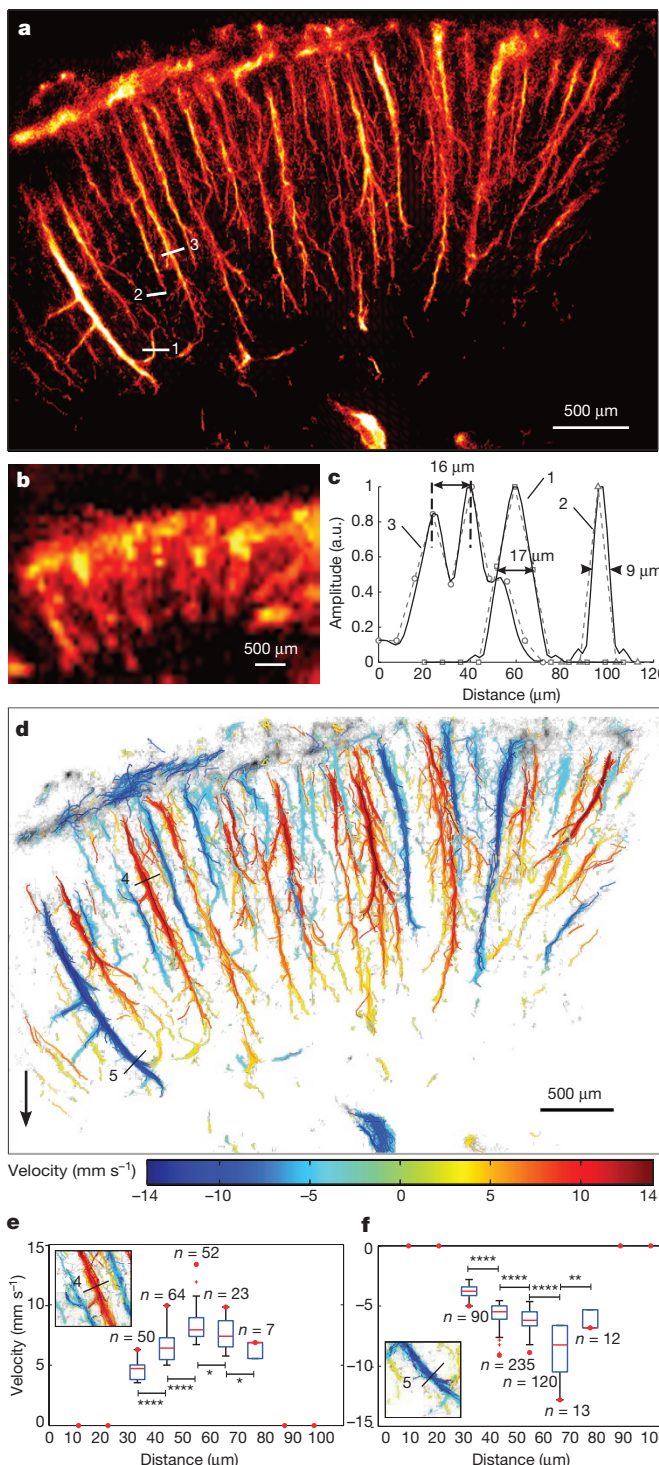


Figure 2 | Spatial resolution and quantification of uULM in the rat brain cortex through a thinned skull window. **a**, Microbubble density maps were reconstructed with a spatial resolution of $\lambda/10$ (pixel size = $8 \mu\text{m} \times 10 \mu\text{m}$). **b**, Same area in a conventional power Doppler image. **c**, Interpolated profiles along the lines marked in **a** display $9 \mu\text{m}$ vessels (2) and resolve two vessels closer than $16 \mu\text{m}$ (3). a.u., arbitrary units. **d**, Dynamic tracking of bubbles separates vessels in two populations with opposite blood flow direction. Positive values indicate blood flow distancing from the probe. Bubble velocities between 1 mm s^{-1} and 14 mm s^{-1} are detectable. **e**, **f**, Velocity profiles associated with lines 4 (**e**) and 5 (**f**) in **d**. Red line, median; blue box, 25th to 75th percentile; whiskers extend to the most extreme data points that are not considered outliers; other points, outliers. Unpaired Student's *t*-test. * $P < 0.05$, ** $P < 0.01$, *** $P < 0.001$, **** $P < 0.0001$.

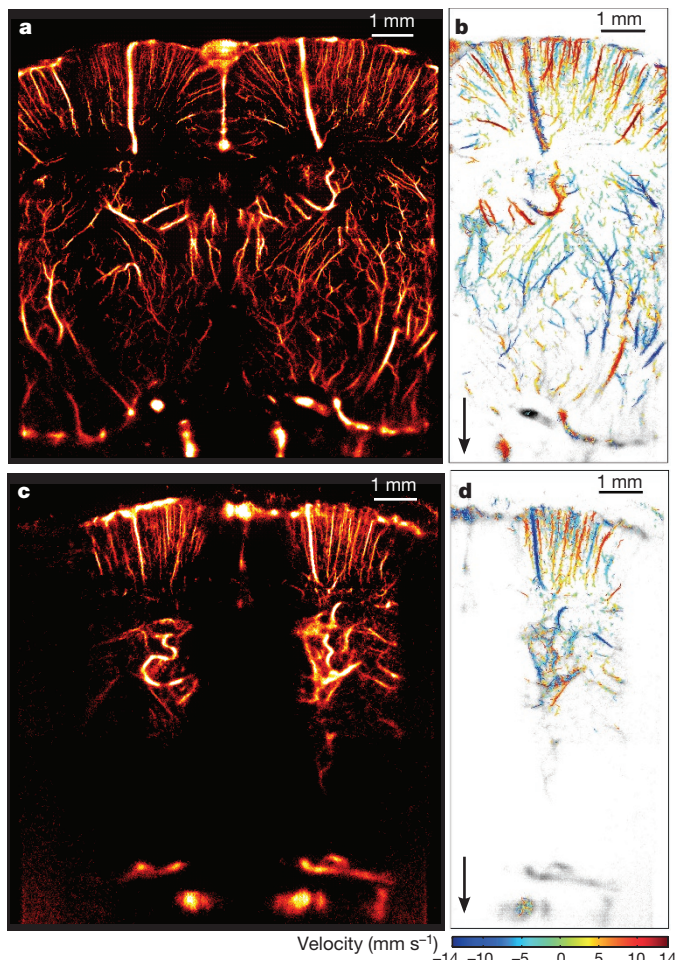


Figure 3 | uULM of the rat brain through a thinned skull window or through the intact skull. **a**, uULM performed through a thinned skull at a coronal section, Bregma -1.5 mm , providing a resolution of $10 \mu\text{m} \times 8 \mu\text{m}$ in depth and lateral direction, respectively. **c**, uULM performed through the intact skull at Bregma -1 mm . Owing to the attenuation of the ultrasound waves in the presence of the bone, the achieved resolution was $12.5 \mu\text{m} \times 1 \mu\text{m}$ in depth and lateral direction, respectively. Thus, the smallest vessel detectable was $20 \mu\text{m}$ wide. **b**, **d**, In-plane velocity maps from parts of the vessels in **a** and **c**, respectively.

to their periphery. Although the images are integrated over a slab of about $100 \mu\text{m}$ thick, we could separate two sets of vessels simply on the basis of their flow velocities. Some bubbles were travelling at a much slower speed in the opposite direction than the background venules. Moreover, in contrast with conventional ultrasound Doppler imaging, which is sensitive mostly to flow towards or away from the ultrasound probe, here we also observed and measured microbubbles that were moving sideways. This is particularly useful to observe the tortuosity of the small vessels and detect abrupt branching in vessels within the cortex.

In-plane velocity measurements can define the resolution of uULM. We consider that two resolution cells are distinguishable if their velocity distributions are statistically different ($P < 0.05$). The median of the upper half of the velocity distribution for each resolution cell is displayed in Fig. 2e, f. When the resolution cells are $8-12 \mu\text{m}$ in size, adjacent pixels can be considered distinct. Interestingly, the maximum velocities follow a parabolic profile, as expected for vessels of this size.

Finally, we investigated the spatial coverage of our imaging method. At 15 MHz, the attenuation of an ultrasound wave within brain tissue is approximately 5 dB cm^{-1} (ref. 23), which allows imaging at several centimetres depth. Super-resolved images could be obtained

in vivo over the entire depth of the brain (12.5 mm at Bregma –1.5 mm; Fig. 3a), demonstrating that ULM can map vessels below the rat brain cortex over several coronal planes (Extended Data Fig. 2). Super-resolved imaging is also possible through the intact skull (Fig. 3c; Bregma –1.0 mm) but the lower signal-to-noise ratio, resulting from skull-induced signal attenuation, globally reduces the number of localized microbubbles, increasing the limit of the smallest detectable vessel. However, this non-invasive version of our imaging method can still detect vessels that are 20 μm wide and distinguish vessels that are 20 μm apart deep into the brain (>8 mm). In the future, the resolution could be further improved by localizing the microbubbles directly from radio-frequency data, which could also allow the correction of aberrations from the skull^{24,25}.

In conventional clinical ultrasound imaging applications, resolution is inherently correlated to the ultrasonic frequency and, consequently, is inversely correlated to penetration depth. However, in uULM, resolution is related to the signal-to-noise ratio, the bandwidth of backscattered echoes and the number of array elements used in the beamforming process. This indicates that very high resolution could be reached, even deep into organs, in clinical applications. As microbubbles are clinically approved contrast agents and our acoustic parameters are well within the US Food and Drug Administration guidelines, such clinical applications could be rapidly implemented with conventional transducers. For these reasons, it is conceivable that dynamic images of the human brain vasculature could be achieved with lower frequency ultrasound (around 1 MHz) that can penetrate the skull. Ultrafast ultrasound localization could also be applied to other deep-seated organs such as liver, kidney or breast, currently imaged with ultrasound by implementing appropriate motion-correction algorithms. Such algorithms can be performed through image registration based on the cross-correlation of the radio-frequency signal acquired at high frame rates, which can detect motion at the micrometric scale^{5,14,15}. The microbubble events necessary for uULM can then be motion compensated thanks to this co-registered image. Consequently, this technique will probably have an important impact on the study and diagnostics of normal biological processes or diseases such as tumour-related angiogenesis.

We demonstrate super-resolution images of rat brain microvessels with pixel sizes comparable to the size of red blood cells, indicating that vessels ten times smaller than the ultrasonic wavelength can be mapped. Since ultrafast localization imaging can be performed through the skull, non-invasive longitudinal studies may be envisioned in the future over single or multiple planes within very reasonable acquisition times in preclinical or clinical studies. ULM, by removing the diffraction-induced trade-off between resolution and penetration of ultrasound waves, emerges as the first *in vivo* technique for imaging and quantifying blood flow at microscopic resolution deep into living organs.

Online Content Methods, along with any additional Extended Data display items and Source Data, are available in the online version of the paper; references unique to these sections appear only in the online paper.

Received 12 June; accepted 30 September 2015.

1. Hell, S. W. & Wichmann, J. Breaking the diffraction resolution limit by stimulated emission: stimulated-emission-depletion fluorescence microscopy. *Opt. Lett.* **19**, 780–782 (1994).
2. Betzig, E. *et al.* Imaging intracellular fluorescent proteins at nanometer resolution. *Science* **313**, 1642–1645 (2006).

3. Huang, B., Babcock, H. & Zhuang, X. Breaking the diffraction barrier: super-resolution imaging of cells. *Cell* **143**, 1047–1058 (2010).
4. Tanter, M. & Fink, M. Ultrafast imaging in biomedical ultrasound. *IEEE Trans. Ultrason. Ferroelectr. Freq. Control* **61**, 102–119 (2014).
5. Couture, O., Tanter, M. & Fink, M. Method and device for ultrasound imaging. Patent Cooperation Treaty (PCT)/FR2011/052810 (2010).
6. Desailly, Y., Couture, O., Fink, M. & Tanter, M. Sono-activated ultrasound localization microscopy. *Appl. Phys. Lett.* **103**, 174107 (2013).
7. Couture, O. *et al.* Ultrafast imaging of ultrasound contrast agents. *Ultrasound Med. Biol.* **35**, 1908–1916 (2009).
8. Chugh, B. P. *et al.* Measurement of cerebral blood volume in mouse brain regions using micro-computed tomography. *Neuroimage* **47**, 1312–1318 (2009).
9. Huang, C.-H. *et al.* High-resolution structural and functional assessments of cerebral microvasculature using 3D Gas ΔR_2^* -mMRA. *PLoS One* **8**, e78186 (2013).
10. Hong, G. *et al.* Multifunctional *in vivo* vascular imaging using near-infrared II fluorescence. *Nature Med.* **18**, 1841–1846 (2012).
11. Yao, J. *et al.* High-speed label-free functional photoacoustic microscopy of mouse brain in action. *Nature Methods* **12**, 407–410 (2015).
12. Gessner, R. C., Frederick, C. B., Foster, F. S. & Dayton, P. A. Acoustic angiography: a new imaging modality for assessing microvasculature architecture. *Int. J. Biomed. Imaging* **2013**, 936593 (2013).
13. Demene, C. *et al.* Spatiotemporal clutter filtering of ultrafast ultrasound data highly increases Doppler and fUltrasound sensitivity. *IEEE Trans. Med. Imaging* **PP**, 2271–2285 (2015).
14. Tanter, M., Bercoff, J., Sandrin, L. & Fink, M. Ultrafast compound imaging for 2-D motion vector estimation: application to transient elastography. *IEEE Trans. Ultrason. Ferroelectr. Freq. Control* **49**, 1363–1374 (2002).
15. Denarie, B. *et al.* Coherent plane wave compounding for very high frame rate ultrasonography of rapidly moving targets. *IEEE Trans. Med. Imaging* **32**, 1265–1276 (2013).
16. Viessmann, O. M., Eckersley, R. J., Christensen-Jeffries, K., Tang, M. X. & Dunsby, C. Acoustic super-resolution with ultrasound and microbubbles. *Phys. Med. Biol.* **58**, 6447–6458 (2013).
17. Christensen-Jeffries, K., Browning, R. J., Tang, M.-X., Dunsby, C. & Eckersley, R. J. *In vivo* acoustic super-resolution and super-resolved velocity mapping using microbubbles. *IEEE Trans. Med. Imaging* **34**, 433–440 (2015).
18. Paxinos, G. & Watson, C. *The Rat Brain in Stereotaxic Coordinates* 6th edn (Academic, 2006).
19. Szabo, T. L. in *Diagnostic Ultrasound Imaging* (ed. Szabo, T. L.) 337–380 (Academic, 2004).
20. Mishra, A. *et al.* Imaging pericytes and capillary diameter in brain slices and isolated retinae. *Nature Protocols* **9**, 323–336 (2014).
21. Itoh, Y. & Suzuki, N. Control of brain capillary blood flow. *J. Cereb. Blood Flow Metab.* **32**, 1167–1176 (2012).
22. Kamoun, W. S. *et al.* Simultaneous measurement of RBC velocity, flux, hematocrit and shear rate in vascular networks. *Nature Methods* **7**, 655–660 (2010).
23. Goss, S. A., Frizzell, L. A. & Dunn, F. Ultrasonic absorption and attenuation in mammalian tissues. *Ultrasound Med. Biol.* **5**, 181–186 (1979).
24. Pernot, M., Montaldo, G., Tanter, M. & Fink, M. ‘Ultrasonic stars’ for time-reversal focusing using induced cavitation bubbles. *Appl. Phys. Lett.* **88**, 034102 (2006).
25. O'Reilly, M. A. & Hynynen, K. A super-resolution ultrasound method for brain vascular mapping. *Med. Phys.* **40**, 110701 (2013).

Supplementary Information is available in the online version of the paper.

Acknowledgements This work was supported principally by the Agence Nationale de la Recherche (ANR), within the project ANR MUSLI. We thank the Fondation Pierre-Gilles de Gennes for funding C.E. The laboratory was also supported by LABEX WIFI (Laboratory of Excellence ANR-10-LABX-24) within the French Program “Investments for the Future” under reference ANR-10-IDEX-0001-02 PSL*.

Author Contributions C.E., J.P., S.P., Z.L., O.C. and M.T. designed the experiments; C.E. and S.P. performed the experiments; C.E., J.P. and O.C. analysed the data; Y.D., O.C. and M.T. performed the theoretical analysis. All the authors discussed the results and wrote the paper.

Author Information Reprints and permissions information is available at www.nature.com/reprints. The authors declare competing financial interests: details are available in the online version of the paper. Readers are welcome to comment on the online version of the paper. Correspondence and requests for materials should be addressed to M.T. (mickael.tanter@espci.fr).

METHODS

Theoretical resolution limit. The given theoretical resolution limit corresponds to the position error of the localization process⁶. This PSF deconvolution for single isolated spots is inherently limited by the number of channels used in receive processing and the timing resolution of the acquisition system. The latter is limited mainly by the sampling frequency of the echoes before beamforming. An approximate value for the theoretical resolution limit in the axial dimension can be obtained by propagating the sampling error in a time-of-flight model, which yields:

$$\sigma_{z0} \approx c\sigma_\tau/(2n^{1/2})$$

where σ_{z0} is the localization error in the axial dimension, c is the sound speed, σ_τ is the timing resolution of the system and n is the number of channels used in receive processing. Note that the lower limit of the timing resolution is linked to the Cramer–Rao lower bound (CRLB), which describes the minimum obtainable estimation error variance when using an unbiased estimator. The derivation of the CRLB was given by Walker and Trahey for ultrasound²⁶. For tasks related to ultrasonic displacement estimation. The standard deviation σ_τ of arrival time estimates compared to the theoretical one is described by the relation:

$$\sigma_\tau = \sigma(\hat{\tau}_0 - \tau_0) \geq \sqrt{\frac{3}{2f_0^3\pi^2T(B^3 + 12B)} \left(\frac{1}{\rho^2} \left(1 + \frac{1}{\text{SNR}^2} \right)^2 - 1 \right)}$$

where f_0 is the transmit pulse centre frequency, B is the pulse bandwidth, T is the kernel size for the time delay estimation, ρ is the normalized correlation between signals (that is, the correlation between the experimental signal and the reference signal used for the PSF decorrelation), and SNR is the signal-to-noise ratio of receive signals.

For the lateral resolution, the size of the aperture must also be taken into account as in any classical imaging modality:

$$\sigma_{x0} \approx 2 \times 3^{1/2} c\sigma_\tau f/(Dn^{1/2})$$

where σ_{x0} is the localization error in the lateral dimension, f is the focal length and D is the length of the transducer array (which is the imaging aperture here). Following these theoretical models, it is predicted that the 15 MHz array used in this study could attain a maximum resolution (full-width at half-maximum) of 2.5 μm in the axial direction and 5 μm in the lateral direction at 1 cm depth. In humans, lower frequencies are exploited to attain 10 cm penetration. With the same theoretical model, we can predict a 6 μm isotropic resolution with a current transducer matrix (32 \times 32 elements, 300 μm spatial pitch, 2.5 MHz frequency, 70% frequency bandwidth, $\rho > 0.9$, 12 dB SNR at 5 cm depth).

Animals. All experiments were performed in agreement with the European Community Council Directive of 22 September 2010 (010/63/UE) and the local ethics committee (Comité d'éthique en matière d'expérimentation animale no. 59, C2EA-59, 'Paris Centre et Sud'). Accordingly, the number of animals in our study was kept to the necessary minimum. Experiments were performed on $n = 3$ male Sprague–Dawley rats (Janvier Labs), weighing 200–225 g at the beginning of the experiments. Animals arrived in the laboratory 1 week before the beginning of the experiment, and were housed three per cage. They were kept at a constant temperature of 22 °C, with a 12 h alternating light/dark cycle (light 7 a.m. to 7 p.m.). Food and water were available *ad libitum*.

Preparation of the thinned-skull imaging windows. The skull of the rats was thinned to 75–100 μm over an area of approximately 0.6 cm \times 0.9 cm. The thinned window suits the dimension of the ultrasound linear array (0.08 mm per element; 128 elements = 10.24 mm width). The surgical procedure was performed 1–2 days before imaging under anaesthesia using intraperitoneal injections of medetomidine (Domitor; 0.3 mg kg⁻¹) and ketamine (Imalgène; 40 mg kg⁻¹). The head of the animal was placed in a stereotaxic frame and the skull bone was drilled (Foredom) at low speed with a micro drill steel burr (Fine Science Tools, catalogue no. 19007-07). To prevent swelling, or oedema of the cerebral cortex, the skull was frequently cooled with saline and an airstream during the thinning procedure as described previously²⁷. The thinned window was protected by a small (1 cm \times 1 cm) plastic cover, and the skin was sutured using 5.0 non-absorbable Ethicon thread. Preliminary experiments showed that this method enabled good quality ultrasound imaging results within 24 h to 3 days after the preparation, as the bone tends to re-grow.

Preparation of ultrasound contrast-agent microbubbles. To reconstruct the vascular microstructure of the rat brain, 1–5 μm perfluorocarbon-filled microbubbles (Bracco) were dissolved with 0.9% NaCl to yield an initial concentration of 2×10^8 microbubbles per ml. This concentration corresponds to approximatively

500,000 bubbles per ml of blood per injection, which corresponds to the maximal dose injected in clinical practice for superficial contrast-enhanced ultrasound²⁸. Ultrafast ultrasound localization microscopy was performed in the brain by injecting a maximum of 18 bolus injections (corresponding to 2.7 ml of the initial suspension) through the catheterized jugular vein. The coronal ultrafast acquisitions of the brain were performed every 15 min to guarantee that the injected boluses had been cleared out.

Ultrafast ultrasound imaging sequence. Ultrasound imaging was performed using ultrafast Doppler imaging based on compounded plane-wave ultrasound transmissions^{29,30}. The hardware of the ultrasound scanner was not modified. Ultrafast sequences were initiated and processed through software-based sequence encoding and data were imported through a PCI-Xpress fast bus for GPU-based post-treatment.

Owing to its high spatiotemporal resolution (1 ms, 100 μm) (ref. 31), this technique can measure small haemodynamic changes related to the neurovascular coupling. Real-time B-mode imaging was used to control the placement of the probe on the field of view. In detail, we developed a plane-wave compounded ultrafast imaging sequence (three tilted plane waves, -3° , 0° and 3° , pulse-repetition frequency PRF = 1,500 Hz) to perform a scan of the entire brain and have a detailed overview of its microvasculature over different coronal imaging planes at a high frame rate (500 Hz). Our ultrasonic probe is a custom-built array with 160 elements and a central frequency of 20.3 MHz (pitch = 0.08 mm, elevation focus = 10 mm). Its 15.4 MHz bandwidth allowed the use of this probe at a frequency of 15 MHz. The signal from the 16 elements on either side is discarded as it is mounted on a fully programmable ultrasound clinical scanner with 256 channels in transmission and 128 parallel channels in reception. Data are transferred using a 16 \times , 6 Gb s⁻¹ PCI express bus and processed using a 12-core 3 GHz Xeon processor, NVidia Quadro K5000 Graphical Processing Unit with a bus at 173 Gb s⁻¹, providing 2.1 teraflops. Such software-based architecture enables programming of custom transmit/receive sequences where the frame rate of each acquisition can reach more than 20 KHz. The linear array was coronally fixed at the anterior–posterior coordinates of Bregma -0.5 mm and coronally translated for 500 μm with a motor to scan and retrieve the vasculature of the whole brain along 2 cm. Each pressure transmit pulse consists of 6 cycles (2 μs duration at 15 MHz) at a 1.5 MPa peak rarefaction acoustic pressure (mechanical index = 0.4). These pressure amplitudes are chosen to reduce the ultrasound-induced disruption of microbubbles and to allow the tracking of these agents over several images.

Boluses of 150 μl microbubbles were injected at the beginning of each ultrafast acquisition. Once the scan was completed, we fixed the probe above the Bregma -1.0 mm to continuously insonify for 150 s the rat cortex (3.5 mm depth). Ten minutes of acquisition were required per each coronal plane of the whole-brain scan (11.6 mm depth). In this latter case, we injected two 150 μl boluses of contrast agents (at the beginning of the ultrafast acquisition and in the middle, 5 min) to avoid a drop in the microbubble concentration due to the dynamic of the boluses. The backscattered echoes were recorded, beamformed with λ -line spacing and coherently added to produce an echographic image at each transmission. Successive raw images corresponding to three different transmission angles at 1,500 Hz PRF are then coherently added to produce one higher-contrast ultrasonic image for each set of tilted angles at a 500 Hz frame rate.

Data treatment for bubble localization. High-pass spatiotemporal filtering was implemented on the stack of the ultrafast images to discriminate the high temporal components, belonging to the blood signal, from the slow-moving tissue. Next, the stack of filtered ultrafast acquisition was rescaled via interpolation, yielding super-resolved output images with a pixel size of 10 $\mu\text{m} \times 8 \mu\text{m}$. Since the bubbles are much smaller than the wavelength (1–3 μm versus 100 μm) and can be individually separated in space and time, they appear as the PSF of the ultrasound system. This PSF is well behaved with respect to the theory of acoustic diffraction because human and animal soft tissues can be considered homogeneous for acoustic properties at first-order approximation³².

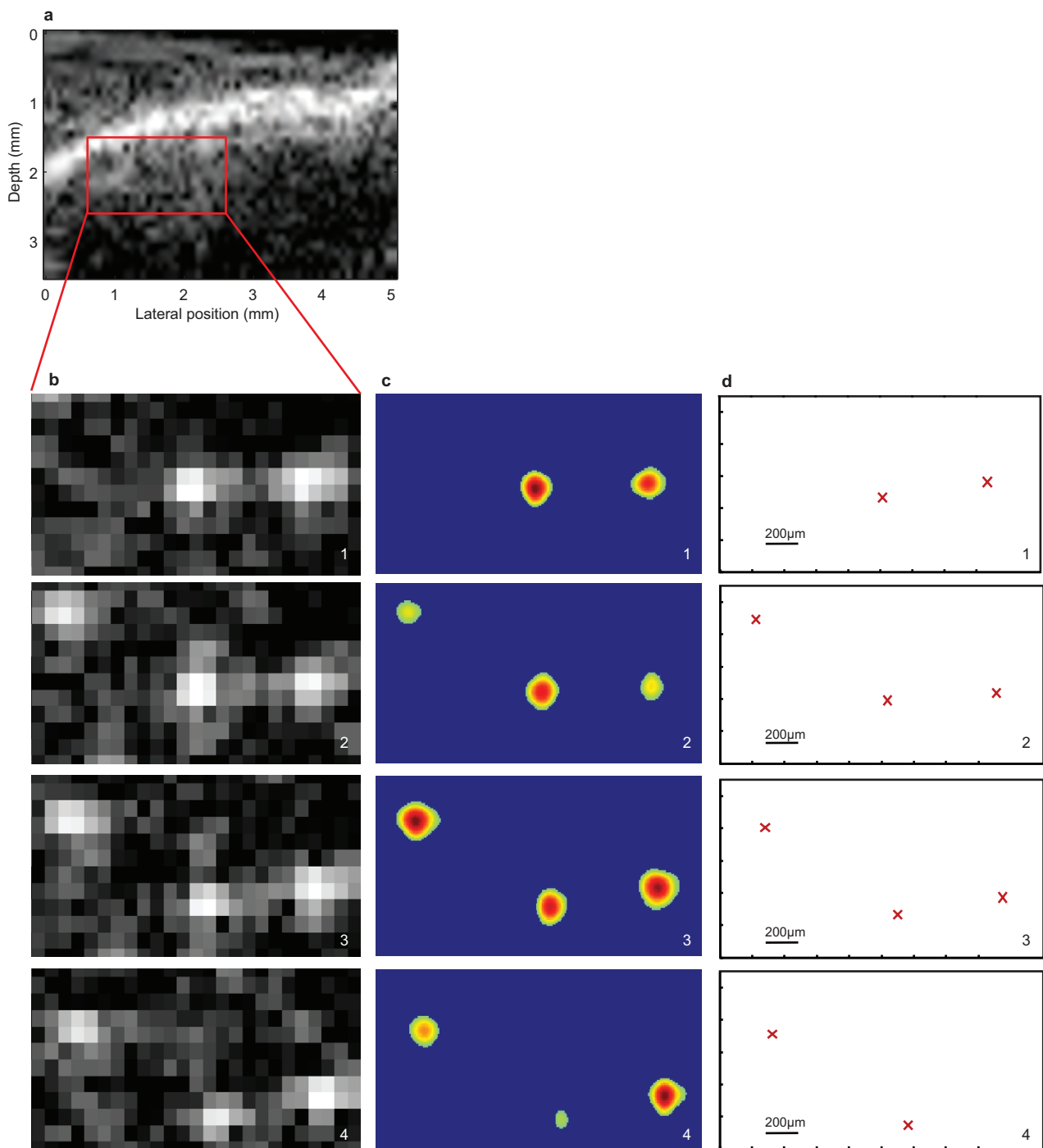
Thereafter, we computed a Gaussian low-pass spatial filter and extracted a two-dimensional PSF for deconvolution of the rescaled ultrafast acquisitions. Hence, each individual bubble was localized, across all frames in the axial position and in depth, with a Gaussian two-dimensional profile whose summit represents the centroid of each separable source (Extended Data Fig. 1). Only 50% of the maximum of the full-width at half-maximum was kept to reconstruct the density maps of the bubbles; such thresholding helped cancel unwanted noisy signals. Additionally, to avoid any artefact corresponding to independent neighbouring bubble events, only bubbles that could be followed for at least 2 ms were included. Eventually the bubbles were counted and grouped according to their closeness. Almost 1.2 million bubbles were counted in the rat cortex within 74,800 frames. Supplementary Video 1 shows the reconstruction of each vessel through the passage of individual microbubbles.

A displacement vector was drawn between these positions, enabling the evaluation of the instantaneous in-plane velocities of the bubbles, computed as the rate

of displacement from one frame to the next frame divided by the time interval. Only tracks composed by more than 5 frames (10 ms) were considered to evaluate the velocities. Coloured velocity maps were constructed using the bubble paths associated with their in-plane velocities (Fig. 2d). More specifically, blue corresponds to the velocities towards the top and the red refers to the in-plane velocities towards the bottom. Taken separately but treated equally, the velocity maps were exploited to retrieve the velocity profiles of each downstream and upstream micro-vessel. In Fig. 2e, we selected two representative vessels: (4) and (5), whose velocities were oriented towards the bottom and towards the top, respectively. We evaluated the number of bubbles in a fixed-resolution cell (Δxz), across the sections of the two chosen vessels, and extracted 50% of the fastest bubbles. Then, we measured the mean \pm standard deviation of each thresholded in-plane velocity vector and performed an unpaired Student's *t*-test. When Δxz was chosen between 8 μm and 12 μm , the quantification of the velocity distribution for each resolution cell gave a result that was statistically different from the adjacent one ($P < 0.05$). Finally, uULM was performed to reconstruct the vascular network and quantify the velocity maps in the whole brain. In Extended Data Fig. 2, we show how the microvasculature of the brain was retrieved with high resolution in depth (11.6 mm) along different coronal imaging planes (from Bregma -0.5 mm to Bregma -4.5 mm). Each of these ultrasound acquisitions was detached in three panels of 4 mm depth to properly filter out the thinned skull bone. Supplementary Video 2 shows the various coronal slices taken during the experiments. It should be

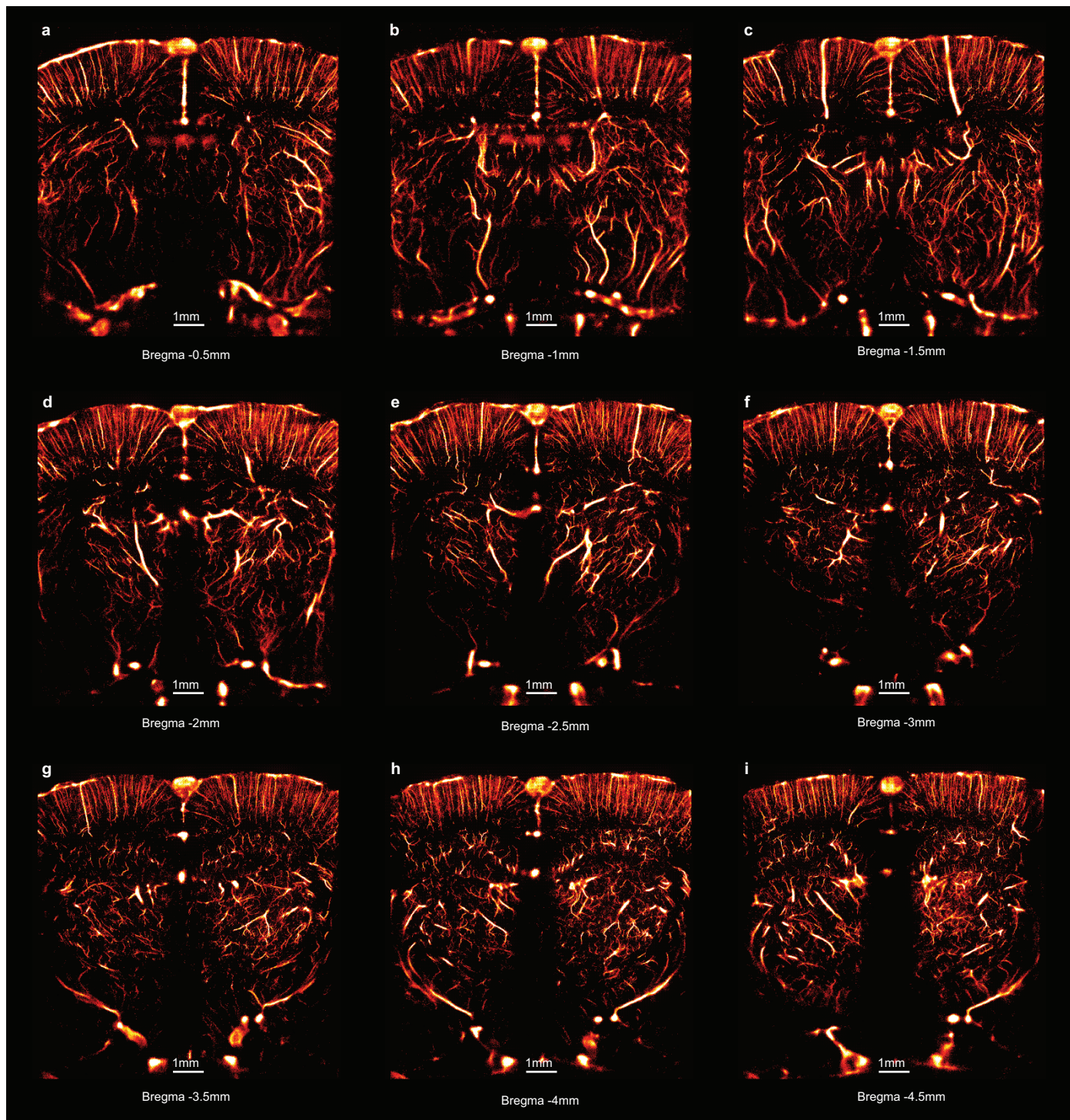
noted that the same filter was applied to reconstruct the vasculature of the cortex in Figs 2a and 3a, and Extended Data Fig. 2a–i. The in-plane velocity maps in Extended Data Fig. 3 were attained with the same data treatment as Figs 2d and 3b. They enable the quantification of velocity distributions in depth in the whole brain, corresponding to the coronal imaging plans in Extended Data Fig. 3.

26. Walker, W. F. & Trahey, G. E. A fundamental limit on delay estimation using partially correlated speckle signals. *IEEE Trans. Ultrason. Ferroelectr. Freq. Control* **42**, 301–308 (1995).
27. Osmanski, B.-F., Pezet, S., Ricobaraza, A., Lenkei, Z. & Tanter, M. Functional ultrasound imaging of intrinsic connectivity in the living rat brain with high spatiotemporal resolution. *Nature Commun.* **5**, 5023 (2014).
28. Dietrich, C. F. *et al.* An EFSUMB introduction into Dynamic Contrast-Enhanced Ultrasound (DCE-US) for quantification of tumor perfusion. *Ultraschall Med.* **33**, 344–351 (2012).
29. Bercoff, J. *et al.* Ultrafast compound Doppler imaging: providing full blood flow characterization. *IEEE Trans. Ultrason. Ferroelectr. Freq. Control* **58**, 134–147 (2011).
30. Errico, C., Osmanski, B.-F., Pezet, S., Couture, O., Lenkei, Z. & Tanter, M. Transcranial functional ultrasound imaging of the brain using microbubble-enhanced ultrasensitive Doppler. *NeuroImage* **124**, 752–761 (2015).
31. Macé, E. *et al.* Functional ultrasound imaging of the brain. *Nature Methods* **8**, 662–664 (2011).
32. Duck, F. A. *Physical Properties of Tissues: A Comprehensive Reference Book* (Academic, 2013).



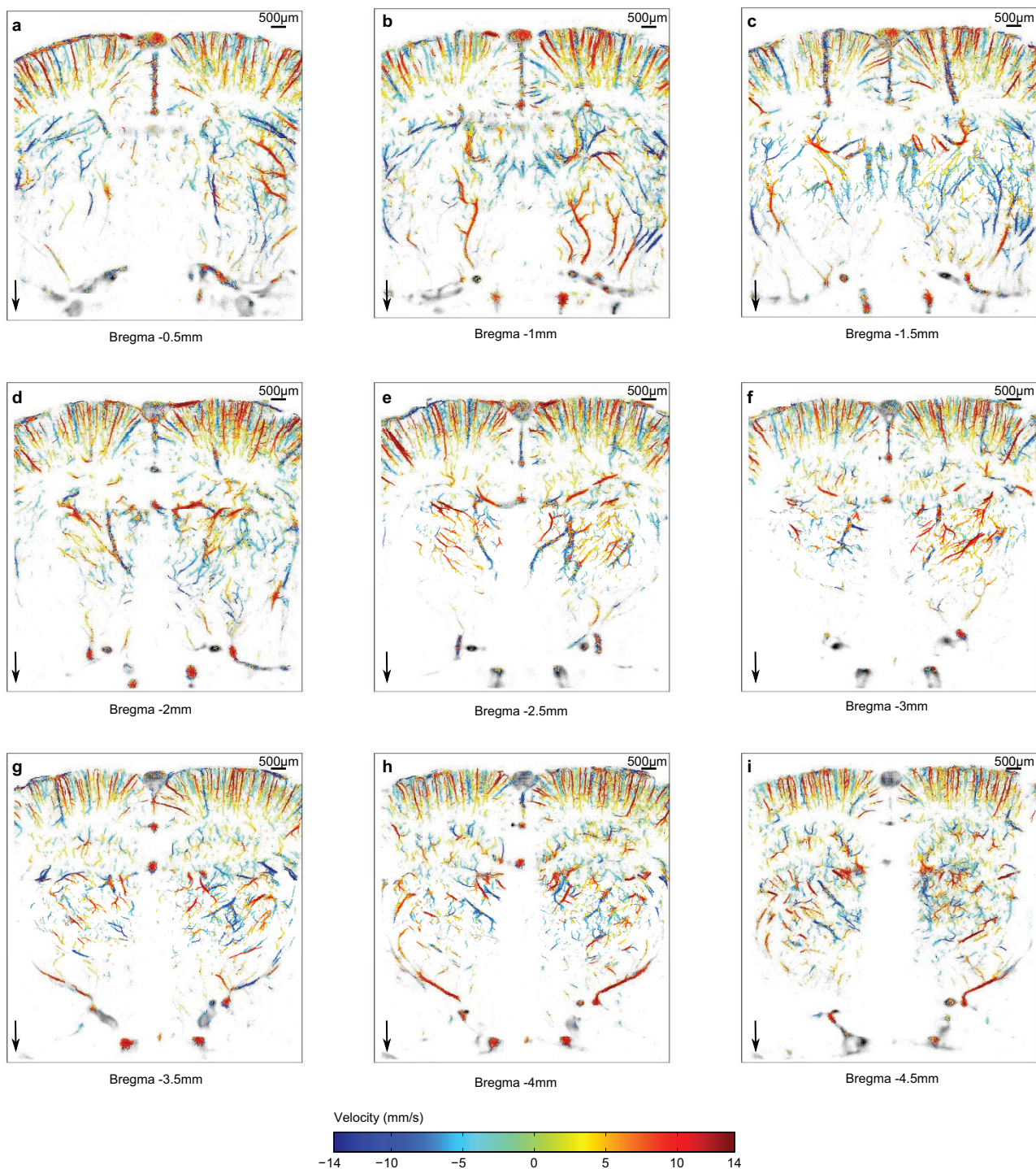
Extended Data Figure 1 | Schema of the temporal and spatial localization of unique sources. **a**, Stack of B-mode images. The region of interest corresponds to a region of $2\text{ mm} \times 1.1\text{ mm}$ within the cortex. **b**, Spatiotemporal filtering of the B-mode images shows the presence of decorrelating microbubbles in each frame (1–4). **c**, The four representative

frames are separated by 44 ms (1–4). **d**, Computed two-dimensional PSF of the rescaled and filtered ultrafast acquisitions. These echoes are then interpolated and the Cartesian coordinates of their centre is obtained (1–4). The summit of each two-dimensional Gaussian profile identifies the centroid of each separable source.



Extended Data Figure 2 | uULM coronal scan (anterior-posterior) of the entire rat brain through a thinned skull window. **a–i**, The ultrasound probe was driven by a micro-step motor to perform uULM on different imaging planes separated by 500 μ m. We reconstructed the

vascularization of the rat brain at the following coordinates: Bregma -0.5 mm (a), -1 mm (b), -1.5 mm (c), -2 mm (d), -2.5 mm (e), -3 mm (f), -3.5 mm (g), -4 mm (h), -4.5 mm (i).



Extended Data Figure 3 | Anterior-posterior scan of in-plane velocity maps of the rat forebrain through a thinned skull window. **a–i**, Velocity maps for the different coronal planes presented in Extended Data Fig. 2.